

Observation of the radiative decay of the $^{229\text{m}}\text{Th}$ nuclear clock isomer

<https://doi.org/10.1038/s41586-023-05894-z>

Received: 20 September 2022

Accepted: 28 February 2023

Published online: 24 May 2023

 Check for updates

Sandro Kraemer^{1,2✉}, Janni Moens³, Michail Athanasakis-Kaklamanakis^{1,4}, Silvia Bara¹, Kjeld Beeks⁵, Premaditya Chhetri¹, Katerina Chrysalidis⁴, Arno Claessens¹, Thomas E. Cocolios¹, João G. M. Correia⁶, Hilde De Witte¹, Rafael Ferrer¹, Sarina Geldhof¹, Reinhard Heinke⁴, Niyusha Hosseini⁵, Mark Huyse¹, Ulli Köster⁷, Yuri Kudryavtsev¹, Mustapha Laatiaoui^{8,9,10}, Razvan Lica^{4,11}, Goele Magchiels³, Vladimir Manea¹, Clement Merckling¹², Lino M. C. Pereira³, Sebastian Raeder^{9,10}, Thorsten Schumm⁵, Simon Sels¹, Peter G. Thirolf², Shandirai Malven Tunhuma³, Paul Van Den Bergh¹, Piet Van Duppen¹, André Vantomme³, Matthias Verlinde¹, Renan Villarreal³ & Ulrich Wahl⁶

The radionuclide thorium-229 features an isomer with an exceptionally low excitation energy that enables direct laser manipulation of nuclear states. It constitutes one of the leading candidates for use in next-generation optical clocks^{1–3}. This nuclear clock will be a unique tool for precise tests of fundamental physics^{4–9}. Whereas indirect experimental evidence for the existence of such an extraordinary nuclear state is substantially older¹⁰, the proof of existence has been delivered only recently by observing the isomer's electron conversion decay¹¹. The isomer's excitation energy, nuclear spin and electromagnetic moments, the electron conversion lifetime and a refined energy of the isomer have been measured^{12–16}. In spite of recent progress, the isomer's radiative decay, a key ingredient for the development of a nuclear clock, remained unobserved. Here, we report the detection of the radiative decay of this low-energy isomer in thorium-229 ($^{229\text{m}}\text{Th}$). By performing vacuum-ultraviolet spectroscopy of $^{229\text{m}}\text{Th}$ incorporated into large-bandgap CaF_2 and MgF_2 crystals at the ISOLDE facility at CERN, photons of 8.338(24) eV are measured, in agreement with recent measurements^{14–16} and the uncertainty is decreased by a factor of seven. The half-life of $^{229\text{m}}\text{Th}$ embedded in MgF_2 is determined to be 670(102) s. The observation of the radiative decay in a large-bandgap crystal has important consequences for the design of a future nuclear clock and the improved uncertainty of the energy eases the search for direct laser excitation of the atomic nucleus.

The ^{229}Th isotope and its low-energy isomer have inspired research for decades and the prospect of developing an optical clock using a nuclear transition has intensified efforts⁵. A particular focus lies on the precise measurement of properties relevant for an optical clock involving the direct laser manipulation of nuclear states¹⁷. Values of the isomer's excitation energy reported in the literature have changed substantially over time¹⁸. Recent measurements using conversion-electron spectroscopy of electrically neutral thorium-229 atoms ($^{229}\text{Th}^0$) resulted in an excitation energy of 8.28(17) eV, corresponding, for radiative decay, to photons of a vacuum wavelength of 149.7(31) nm (ref. 14). Measurements of gamma (γ) ray energy differences of nuclear transitions feeding the isomer and the ground state, using a magnetic microcalorimeter, revealed energies of 8.30(92) and 8.10(17) eV, with an associated vacuum wavelength of 149(17) and 153.1(32) nm, respectively^{15,16}.

A half-life of 7(1) μs has been reported for $^{229\text{m}}\text{Th}^0$ deposited onto a microchannel plate detector, an environment in which electron

conversion is expected to constitute the dominant decay path¹³. Theoretical estimates for the radiative decay half-life vary by an order of magnitude between about 10^3 and 10^4 s (refs. 19–21). For a dominating radiative decay, which is required for the clock application, the non-radiative decay channels, for example, by means of electron conversion decay, need to be sufficiently suppressed. The last requires charged $^{229\text{m}}\text{Th}$ ions to have an electron binding energy larger than the isomer's decay energy.

At present, two different routes towards a nuclear clock are being pursued. These consist of an approach with triply charged thorium ions stored in a radio-frequency ion trap and a solid-state approach with a thorium-doped large-bandgap crystal^{1,5,22–24}. For the latter, theoretical studies suggest that, at specific lattice positions, the conversion-electron decay channel of the isomer is suppressed and the radiative decay channel becomes dominant^{25,26}. Despite various attempts, the observation of the radiative decay of $^{229\text{m}}\text{Th}$ following the

¹KU Leuven, Instituut voor Kern- en Stralingsfysica, Leuven, Belgium. ²Ludwig-Maximilians-Universität München, Garching, Germany. ³KU Leuven, Quantum Solid State Physics, Leuven, Belgium. ⁴CERN, Geneva, Switzerland. ⁵Institute for Atomic and Subatomic Physics, TU Wien, Vienna, Austria. ⁶Centro de Ciências e Tecnologias Nucleares, Departamento de Engenharia e Ciências Nucleares, Instituto Superior Técnico, Universidade de Lisboa, Bobadela, Portugal. ⁷Institut Laue-Langevin, Grenoble, France. ⁸Department Chemie, Johannes-Gutenberg-Universität, Mainz, Germany. ⁹Helmholtz-Institut Mainz, Mainz, Germany. ¹⁰GSI Helmholtzzentrum für Scherionenforschung, Darmstadt, Germany. ¹¹Horia Hulubei National Institute of Physics and Nuclear Engineering, Bucharest, Romania. ¹²imec, Leuven, Belgium. ✉e-mail: sandro.kraemer@kuleuven.be

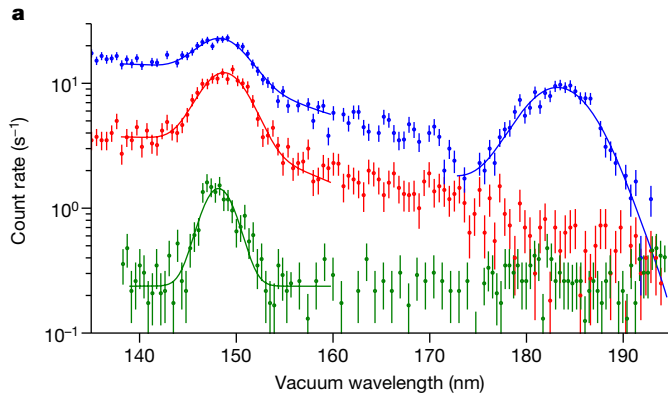


Fig. 1 | Low-resolution wavelength spectra of different crystals. a, b, The spectra are recorded with a 3 mm entrance slit after implantation of $A = 229$ (a) and $A = 230$ (b) beams in a MgF_2 of 5 mm (red), a CaF_2 of 5 mm (blue) and a CaF_2 of 50-nm thick (green) crystal (Extended Data Table 2 and Extended Data Fig. 2). Wavelength data points are recorded for 11 s per grating setting for the 5-mm thick crystals whereas for the 50 nm crystal 23 and 35 s per grating setting are used for the $A = 229$ and $A = 230$ data, respectively. Error bars represent the statistical 1 s.d. uncertainty. The drop in intensity in the $A = 229$

radioactive alpha (α) decay of ^{233}U or the excitation of the nucleus by, for example, synchrotron light has hitherto not been conclusive^{27–30}.

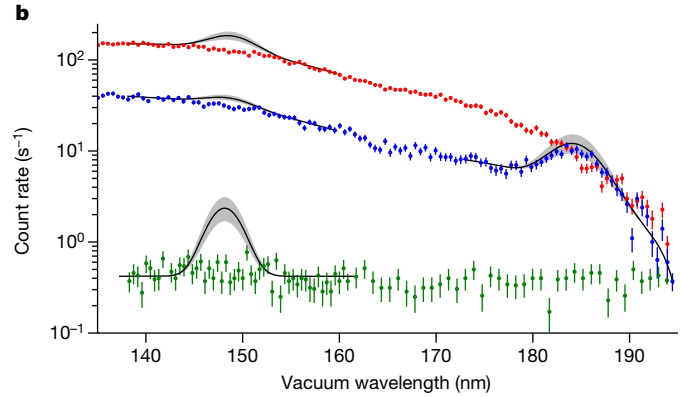
In this work, an alternative approach to produce the ^{229}Th isomer³¹ and thus overcome limitations of previous attempts to detect and characterize its radiative decay is successfully pursued. The isomeric state is populated in the beta (β) decay of ^{229}Ac with a half-life of 62.7(5) min (ref. 32) incorporated in a large-bandgap crystal. This increases the total feeding probability of the isomer by a factor between 7 and 47 compared to the α decay of ^{233}U (ref. 31). The ^{229}Ac sample is obtained from the β -decay chain of ^{229}Fr and ^{229}Ra ion beams implanted in CaF_2 and MgF_2 crystals at 30 keV. Vacuum-ultraviolet (VUV) spectroscopy is performed to study the photon spectrum emitted from the crystals under favourable radioluminescence background conditions, due to the approach of populating the isomer by means of β decay^{28,33}. In addition, emission channelling^{34–36} is used to determine the lattice sites occupied by thorium after implantation of francium and radium, which are expected to play a crucial role in suppressing the conversion-electron decay channel^{25,26}.

Radioactive ion beam production

Radioisotopes are produced at the ISOLDE facility at CERN³⁷ in a nuclear reaction by impinging a 1.4 GeV proton beam on a uranium carbide target heated to about 2,000 °C. The nuclear-reaction products diffuse through the target and effuse towards the ion source, where they are surface-ionized to a singly charged state, subsequently accelerated to 30 keV, separated according to their mass-over-charge ratio using a dipole magnet and transported to the experimental setup. The radioactive ion beam of mass number $A = 229$ is implanted at room temperature into large-bandgap, VUV-transparent CaF_2 ($E_{\text{gap}} = 12.1$ eV, ref. 38) and MgF_2 (12.4 eV, ref. 39) crystals. This results, for CaF_2 (MgF_2), in an implantation depth distribution with a projected range of 17.0 (16.0) nm and a straggling of 3.5 (2.7) nm, respectively⁴⁰. A summary of the properties of the radioactive ion beams and the large-bandgap crystals used for implantation is given in the Methods section, Extended Data Table 1 and Extended Data Table 2, respectively.

VUV spectroscopy

The radioactive beam is implanted into different crystals positioned on a sample holder wheel in the VUV-spectroscopy setup (see Extended Data Fig. 3). High-purity germanium and lanthanum-bromide γ -radiation detectors are placed around the implantation position and



spectrum with the CaF_2 of 5 mm at 172 nm coincides with an outage of the grating control causing a delay in the scanning procedure and resulting in a change of background activity. The solid red, blue and green lines show a fit to the data for the $A = 229$ data. On the basis of a scaling with the implanted activity and assuming that the observed line at 183 nm in the $A = 229$ spectra is due to crystal defects, the black solid line represents the expected signal in the $A = 230$ spectra. The grey uncertainty band includes the 1 s.d. uncertainty on the radioactive ion beam production rates.

used to deduce the beam production rates (Methods and Extended Data Fig. 1) and to determine the total amount of implanted radioisotopes in the crystal. The wheel is rotated after an implantation time between 45 min and 2 h, placing the crystal in front of the entrance slit of a VUV spectrometer (Resonance Ltd, VM180). The distance between the implanted surface of the crystal and the entrance slit is about 3 mm. The spectrometer has a large numerical aperture of $F/1.2$ and houses a plane grating Czerny–Turner mount configuration with off-axis parabolic mirrors. A Hamamatsu R8487 photomultiplier tube detects photons in the wavelength range between 115 and 195 nm. VUV spectra of photons created in the crystals are recorded by rotating the grating, thereby scanning the wavelength and recording the photon count rate in the photomultiplier detector. The instrument operates in the first diffraction order and is calibrated using external calibration light sources (Methods). The efficiency of photon detection for an isotropically emitting point-like source positioned at 3 mm from a 3 mm-wide slit yields about 0.1% at 150 nm (Methods).

The radiative decay of $^{229\text{m}}\text{Th}$ is expected to manifest itself as monochromatic photon emission resulting in a narrow peak around 150 nm in the wavelength spectrum^{14,16}. To observe this signal, VUV spectroscopy is performed on a series of CaF_2 and MgF_2 crystals doped with $A = 229$ and $A = 230$ beams. The $A = 230$ beam implantation is used as a reference measurement, as the ^{229}Th isomer is not populated but where conditions regarding beam intensity and radioluminescence background are similar to those obtained with $A = 229$ beams. Therefore, radiation-induced excitation of electronic modes associated with crystal defects⁴¹ should be observed after implantation of either $A = 229$ and 230 beams into the same crystal whereas the signal from the $^{229\text{m}}\text{Th}$ radiative decay will only appear in the $A = 229$ case.

Typical VUV spectra are shown in Fig. 1. For both types of crystal, MgF_2 and CaF_2 , a peak at 148.7 nm on top of a continuous background is observed in all spectra obtained with the $A = 229$ implanted beam. This 148.7 nm peak is absent in the spectra taken with the $A = 230$ beam. Furthermore, for both the $A = 229$ and $A = 230$ implantations a peak at 183 nm is observed for the 5-mm thick CaF_2 crystal. The continuous background stems from Cherenkov photon emission induced by the β -decay chain of the implanted radioactive isotopes^{33,42} and the constant detector dark-count rate of typically less than 1 Hz. A VUV photon peak can be caused either by the $^{229\text{m}}\text{Th}$ radiative decay or by the radiation-induced excitation of electronic modes associated with crystal defects⁴¹. The latter should be observed for both $A = 229$ and

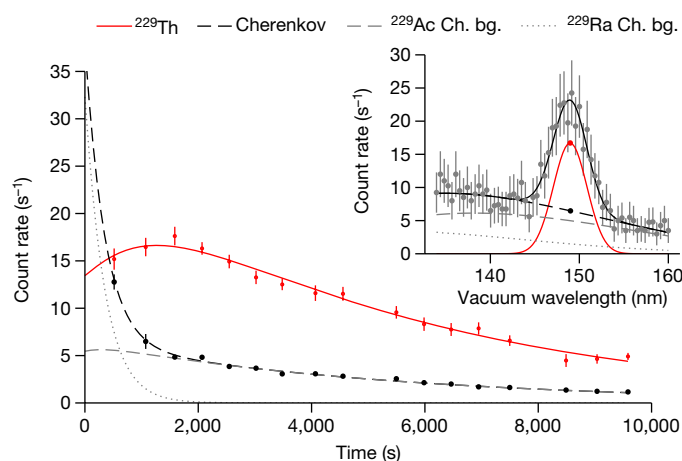


Fig. 2 | Time behaviour of the signal. The fitted peak (red data points) and background (black data points) amplitude count rates of the VUV spectra as a function of time after implantation in the MgF_2 5 mm crystal are shown. Error bars represent the 1 s.d. statistical uncertainty. Coloured lines are the fit result of the data with a differential-equation model of the implantation and decay of the radioactive isotopes from which the half-life of $^{229\text{m}}\text{Th}$ is extracted. The inset shows the fit (solid black line) of the VUV wavelength spectrum (grey data points with 1 s.d. error bars) measured around 1,073 s after implantation to deduce the peak (red circle) and background (black circle) amplitudes. The data were collected using a 2 mm spectrometer entrance slit width and 5 s measurement time per grating setting. The grey dotted and dashed lines represent the contribution of the Cherenkov radiation induced by the β decay of ^{229}Ra and ^{229}Ac , respectively.

$A = 230$ spectra. Assuming that the two VUV photon peaks in the $A = 229$ spectra stem from crystal defects, the expected signal for the $A = 230$ case can be calculated considering the peak intensities in the $A = 229$ spectra and the different instantaneous radiation from the radioactive decays (black lines in Fig. 1). The agreement of the observed intensity for the 183 nm peak in the $A = 229$ and $A = 230$ spectra associates this structure with a CaF_2 crystal defect. The observation of the 148.7 nm peak in the $A = 229$ spectra and its absence in $A = 230$ spectra suggests that these photons are due to the radiative decay of $^{229\text{m}}\text{Th}$.

The time evolution of the intensity of the 148.7 nm photon peak is studied by implanting the $A = 229$ beam in MgF_2 . After 1 hour of implantation, the source is moved in front of the 2 mm entrance slit of the VUV spectrometer and consecutive scans are acquired around the 148.7 nm peak. From the obtained spectra, the 148.7 nm peak and background amplitudes at the peak position are deduced and plotted as a function of time after the end of the implantation period (Fig. 2). The time evolution of the peak amplitude, which is substantially different from its precursor's β decay activity, is compatible with a mother ^{229}Ac -daughter $^{229\text{m}}\text{Th}$ decay sequence. To deduce the $^{229\text{m}}\text{Th}$ half-life from these data, the activities of the full decay chain of ^{229}Fr , ^{229}Ra , ^{229}Ac and $^{229\text{m}}\text{Th}$ are calculated using the half-lives of the first three isotopes known from the literature and the measured beam intensity of ^{229}Fr and ^{229}Ra during the implantation period. By scaling the calculated activity to take into account the total VUV spectrometer efficiency, the isomer feeding probability in the ^{229}Ac β decay and the fraction of radiative to total decaying isomers, a half-life value of 670(102) s for the decay of $^{229\text{m}}\text{Th}$ embedded in a MgF_2 crystal is obtained.

To better constrain the 148.7 nm peak position, scans using small slit sizes are performed. The latter increase the resolution and minimize the influence of the distribution of the implanted radioactive beam in the crystal on the energy uncertainty, at the cost of a decreased efficiency. A typical wavelength scan at 0.5 mm slit size is shown in Fig. 3 (Methods) and the obtained wavelength values from single scans in different crystals and at different slit sizes are shown in Fig. 4.

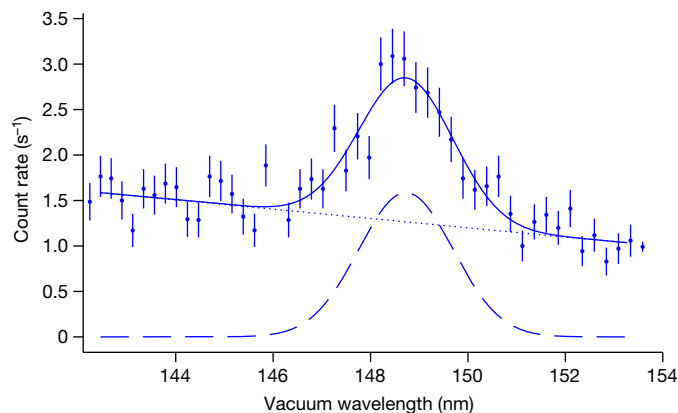


Fig. 3 | Typical high-resolution wavelength spectrum. The data are taken with the CaF_2 5 mm crystal and recorded with an entrance slit width of 0.5 mm, along with a fit (solid line) of the data. Error bars represent the 1 s.d. statistical uncertainty. The scan was started 32 min after the end of the implantation. The dashed line shows the peak signal whereas the dotted line includes the constant dark-count rate (0.3 s^{-1}) and the Cherenkov background contributions. A resolution of 2.25(21) nm full-width at half-maximum was obtained. The resulting wavelength value corresponds to the 11th data value in Fig. 4.

For implantations in MgF_2 , a mean wavelength of 148.688(66) nm is obtained, whereas 5-mm thick and 50-nm thin CaF_2 yield 148.75(13) and 148.623(77) nm, respectively. The stated uncertainties represent only statistical uncertainties from a χ^2 optimization and do not include systematic effects from the calibration procedure.

The observation of the peak at 148.7 nm in both the MgF_2 and CaF_2 crystals with wavelength values within the statistical uncertainty (one σ confidence level), the absence of the signal in measurements using the $A = 230$ decay chain and the time behaviour of the signal's amplitude, leads to the conclusion that the 148.7 nm photons stem from the radiative decay of the $^{229\text{m}}\text{Th}$ isomer.

For the final wavelength value, only measurements with slit settings less than or equal to 0.5 mm are used to limit the systematic uncertainty. The latter accounts for calibration shifts due to different positioning of the wavelength calibration light source and the crystal sample, the distribution of the radioactive source in front of the entrance slit and the reproducibility of the grating position. This leads to a conservative systematic uncertainty of 0.41 nm (Methods). It results in an average wavelength value of 148.71 ± 0.06 (stat.) ± 0.41 (syst.) nm corresponding to an excitation energy of the isomer of 8.338 ± 0.003 (stat.) ± 0.023 (syst.) eV. From the observed rate of the 148.7 nm photons, a lower limit of the fraction of $^{229\text{m}}\text{Th}$ that decays by photon emission can be determined. Using the calculated efficiency of the VUV spectrometer, the deduced production rate of ^{229}Fr and ^{229}Ra , and an estimate of the crystal transmission, a lower limit between 1 and 7% is obtained assuming a total β -feeding probability of the isomer ranging between 93 and 14% (Methods).

Characterization of the lattice location

The VUV results, yielding a lower limit of 1–7% of implanted $^{229\text{m}}\text{Th}$ nuclei decaying by photon emission, indicate that at least several percent of the thorium atoms are incorporated with a local atomic configuration that favours the suppression of conversion-electron decay²⁵. To this end, emission channelling measurements using the radioactive decay radiation (Methods) are performed to characterize the thorium incorporation in the CaF_2 lattice. As the lattice position of implanted thorium ions in CaF_2 cannot be determined using the ^{229}Th isotope because of its long half-life of 7,920 years, ^{231}Th ($T_{1/2} = 25.2 \text{ h}$) is used instead as a proxy. For that purpose, a VUV-grade CaF_2 crystal with a thickness of 0.7 mm is implanted with a beam of mass $A = 231$ at room temperature

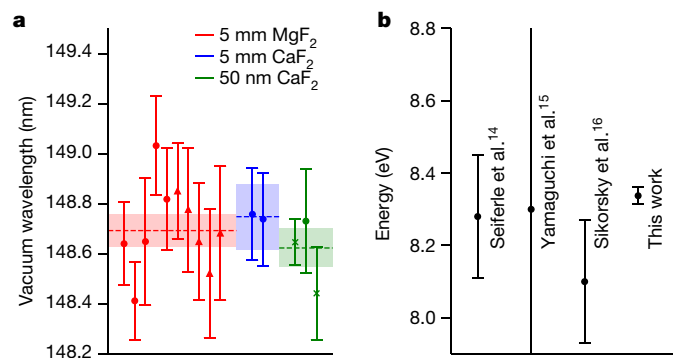


Fig. 4 | Wavelength of the radiative decay and energy of the isomer. a, The results from this work for single wavelength scans with small slit sizes (crosses are 1 mm, circles are 0.5 mm and triangles are 0.25 mm) in three different crystals studied. Uncertainties are 1 s.d. statistical and the weighted average and its uncertainty per crystal is represented by the dashed line and shaded area. **b**, Comparing the energy value deduced from the scans with slits less than or equal to 0.5 mm in all three crystals, including the 1 s.d. statistical and systematic uncertainties, to results of the three most recent studies^{14–16}.

and with a fluence of $10 \times 10^{12} \text{ cm}^{-2}$. Emission channelling patterns of ²³¹Th are measured along four main crystal axes (Fig. 5) after a waiting period of 4 h between the end of the implantation and the start of the measurement, to ensure that spectral contributions from the β decay of the shorter-lived parent isotopes (²³¹Fr, ²³¹Ra and ²³¹Ac) are negligible. To identify and quantify which lattice sites are occupied, measured and simulated emission patterns are numerically fitted⁴³. For that purpose, simulated patterns are calculated for various lattice sites using the Manybeam code³⁴, including Ca and F substitutional sites, as well as various interstitial sites. Each measured pattern is then fitted with one as well as linear combinations of two or three of all the simulated sites from where the respective occupation fractions are obtained. In the present case, if only one occupied site is considered, the best fit is obtained for thorium in a substitutional calcium site (Fig. 5). An occupation fraction of 77(4)% is obtained from the fit. If a linear combination of additional high-symmetry sites for ²³¹Th is considered, the quality of the fit does not improve, indicating that eventual fractions in such sites are below the detection limit (typically of the order of 5%). The calcium substitutional fraction deduced from the fit needs to be corrected for secondary electrons from the sample and internal setup parts⁴³, leading to a final substitutional fraction between 77 and 100%.

The root mean square (r.m.s.) displacement of the ²³¹Th atoms with respect to the calcium site is also obtained from the fit, yielding 0.20(3) Å. The fact that the r.m.s. displacement is substantially larger than the expected thermal vibration amplitude of a thorium atom in CaF₂ (0.08 Å, calculated on the basis of the mass-defect model and the Debye temperature of CaF₂), indicates that additional defects, such as vacancies and self-interstitials, are present in the neighbourhood of the thorium atoms. Such defects are formed in the collision cascades of the implanted ions⁴⁴. The trapping of such defects in the neighbourhood of the thorium atoms may be enhanced by charge compensation mechanisms, for example, the energetically favoured trapping of two interstitial fluorine atoms²⁵. Such charge-compensated configurations are predicted to preserve the large bandgap and thus suppress the conversion-electron decay of the ^{229m}Th isomer²⁵.

Discussion and conclusion

The obtained excitation energy of the isomer is consistent with results from previous studies (Fig. 4). Our value is in agreement within the one σ confidence interval from conversion-electron spectroscopy reported in ref. 14 and one σ and two σ confidence intervals of the recent microcalorimetric measurements in refs. 15 and 16, respectively. It decreases

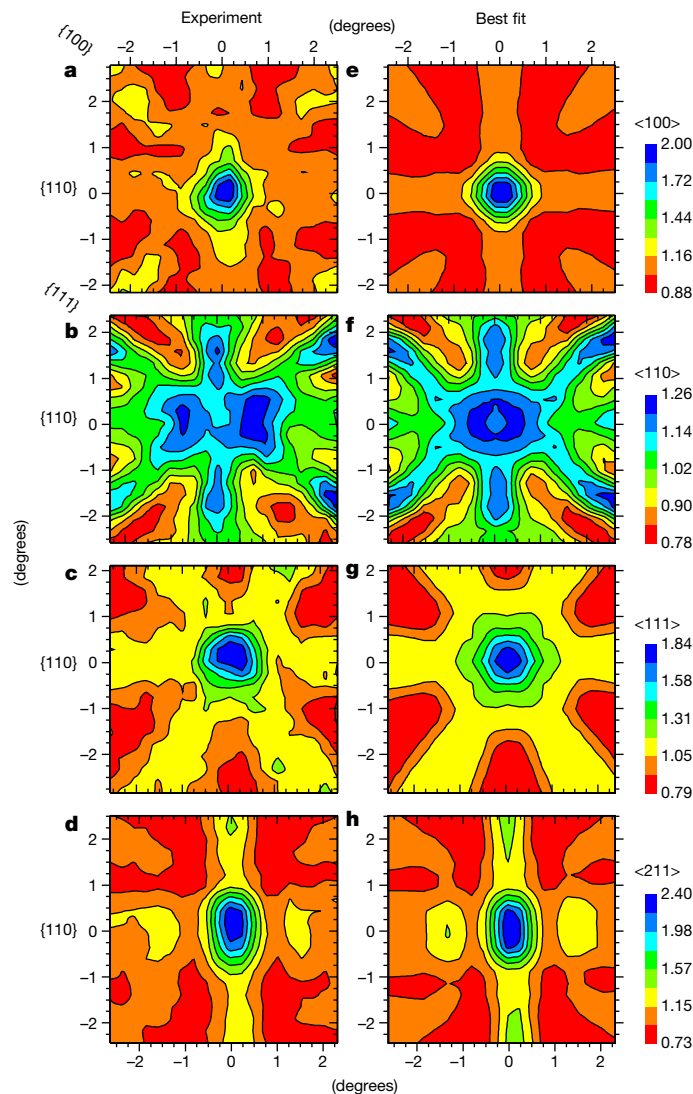


Fig. 5 | Emission channelling patterns of electrons. a–d, Normalized observed patterns from ²³¹Th in CaF₂ following room temperature implantation, in the vicinity of four main crystallographic axes are shown on the left: $\langle 100 \rangle$ (a), $\langle 110 \rangle$ (b), $\langle 111 \rangle$ (c) and $\langle 211 \rangle$ (d). **e–h**, The corresponding best single-site fit with simulated patterns corresponding to calcium substitutional sites is shown on the right: $\langle 100 \rangle$ (e), $\langle 110 \rangle$ (f), $\langle 111 \rangle$ (g) and $\langle 211 \rangle$ (h).

the uncertainty of the isomer's excitation energy by more than a factor of seven compared to each of the two most precise studies available in literature^{14,16}.

The measured half-life value of ^{229m}Th embedded in a MgF₂ crystal is lower compared to the calculated boundaries of the ^{229m}Th half-life^{19–21,45}, but should be considered as a lower limit because of the potential presence of non-radiative decay channels. Moreover, it should be corrected for the refractive index dependence of the crystal environment^{19,46}. Applying a n^3 dependence using the half-life value determined for ^{229m}Th embedded in a MgF₂ crystal and assuming a refractive index of $n = 1.488$ at 148.7 nm a half-life of $2.21(34) \times 10^3 \text{ s}$ can be inferred. Given the shallow implantation depth of the present samples, the validity of the n^3 dependence needs further investigation obtaining more precise half-life values and performing implantation under different conditions and in different crystals.

In conclusion, an alternative approach to populate and study the ²²⁹Th isomer by means of the β decay of ²²⁹Ac incorporated in large-bandgap MgF₂ and CaF₂ crystals through implantation, allowed for the first time to observe the radiative decay of ^{229m}Th. A more precise energy value

of the isomer was determined and the half-life of $^{229\text{m}}\text{Th}$ embedded in MgF_2 was reported. The observed incorporation of thorium in predominantly calcium substitutional sites, favouring the suppression of conversion-electron decay, is consistent with the VUV-spectroscopy results that yield a conservative lower limit of 1–7% for the fraction of $^{229\text{m}}\text{Th}$ that decays by photon emission. The observation of the radiative decay in a solid-state environment marks an important step towards the realization of a nuclear clock. Future studies combining emission channelling and VUV spectroscopy, varying implantation and annealing parameters, and exploring different large-bandgap host crystals, will enable further optimization of this new approach. In particular, further development of the VUV-spectroscopy instrumentation will allow to decrease the uncertainty of the energy value by a factor of up to four and to study the isomer's half-life in different crystals, under different implantation conditions, providing valuable input in the search for laser excitation of the atomic nucleus.

Online content

Any methods, additional references, Nature Portfolio reporting summaries, source data, extended data, supplementary information, acknowledgements, peer review information; details of author contributions and competing interests; and statements of data and code availability are available at <https://doi.org/10.1038/s41586-023-05894-z>.

- Peik, E. & Tamm, C. Nuclear laser spectroscopy of the 3.5 eV transition in Th-229. *Euro. Phys. Lett.* **61**, 181 (2003).
- Campbell, C. J. et al. Single-ion nuclear clock for metrology at the 19th decimal place. *Phys. Rev. Lett.* **108**, 120802 (2012).
- Beeks, K. et al. The thorium-229 low-energy isomer and the nuclear clock. *Nat. Rev. Phys.* **3**, 238–248 (2021).
- Flambaum, V. V. Enhanced effect of temporal variation of the fine structure constant and the strong interaction in ^{229}Th . *Phys. Rev. Lett.* **97**, 092502 (2006).
- Peik, E. et al. Nuclear clocks for testing fundamental physics. *Quant. Sci. Technol.* **6**, 034002 (2021).
- Uzan, J.-P. Varying constants, gravitation and cosmology. *Living Rev. Relativ.* **14**, 2 (2011).
- Derevianko, A. & Pospelov, M. Hunting for topological dark matter with atomic clocks. *Nat. Physics* **10**, 933–936 (2014).
- Arvanitaki, A., Huang, J. & Van Tilburg, K. Searching for dilaton dark matter with atomic clocks. *Phys. Rev. D* **91**, 015015 (2015).
- Thirolf, P. G., Seiferle, B. & von der Wense, L. Improving our knowledge on the $^{229\text{m}}\text{Th}$ isomer: toward a test bench for time variations of fundamental constants. *Ann. Phys.* **531**, 1800381 (2019).
- Kroger, L. A. & Reich, C. W. Features of the low-energy level scheme of ^{229}Th as observed in the alpha-decay of ^{233}U . *Nucl. Phys. A* **259**, 29–60 (1976).
- von der Wense, L. et al. Direct detection of the ^{229}Th nuclear clock transition. *Nature* **533**, 47–51 (2016).
- Thielking, J. et al. Laser spectroscopic characterization of the nuclear-clock isomer $^{229\text{m}}\text{Th}$. *Nature* **556**, 321–325 (2018).
- Seiferle, B., von der Wense, L. & Thirolf, P. G. Lifetime measurement of the $^{229\text{m}}\text{Th}$ nuclear isomer. *Phys. Rev. Lett.* **118**, 042501 (2017).
- Seiferle, B. et al. Energy of the ^{229}Th nuclear clock transition. *Nature* **573**, 243–246 (2019).
- Yamaguchi, A. et al. Energy of the ^{229}Th nuclear clock isomer determined by absolute γ -ray energy difference. *Phys. Rev. Lett.* **123**, 222501 (2019).
- Sikorsky, T. et al. Measurement of the ^{229}Th isomer energy with a magnetic microcalorimeter. *Phys. Rev. Lett.* **125**, 142503 (2020).
- Matinyan, S. Lasers as a bridge between atomic and nuclear physics. *Phys. Rep.* **298**, 199–249 (1998).
- von der Wense, L. & Seiferle, B. The ^{229}Th isomer: prospects for a nuclear optical clock. *Eur. Phys. J. A* **56**, 277 (2020).
- Tkalya, E. V., Schneider, C., Jeet, J. & Hudson, E. R. Radiative lifetime and energy of the low-energy isomeric level in Th-229. *Phys. Rev. C* **92**, 054324 (2015).
- Minkov, N. & Pálffy, A. Reduced transition probabilities for the gamma decay of the 7.8 eV isomer in ^{229}Th . *Phys. Rev. Lett.* **118**, 212501 (2017).
- Ruchowska, E. et al. Nuclear structure of ^{229}Th . *Phys. Rev. C* **73**, 044326 (2006).
- Campbell, C. J., Radnaev, A. G. & Kuzmich, A. Wigner crystals of for optical excitation of the nuclear ^{229}Th isomer. *Phys. Rev. Lett.* **106**, 223001 (2011).
- Rellergert, W. G. et al. Constraining the evolution of the fundamental constants with a solid-state optical frequency reference based on the ^{229}Th nucleus. *Phys. Rev. Lett.* **104**, 200802 (2010).
- Kazakov, G. A. et al. Performance of a ^{229}Th Thorium solid-state nuclear clock. *New J. Phys.* **14**, 083019 (2012).
- Dessovic, P. et al. ^{229}Th -doped calcium fluoride for nuclear laser spectroscopy. *J. Phys. Condens. Matter* **26**, 105402 (2014).
- Pimon, M. et al. DFT calculation of ^{229}Th -doped magnesium fluoride for nuclear laser spectroscopy. *J. Phys. Condens. Matter* **32**, 255503 (2020).
- Stellmer, S. et al. Toward an energy measurement of the internal conversion electron in the deexcitation of the ^{229}Th isomer. *Phys. Rev. C* **98**, 014317 (2018).
- Stellmer, S., Schreitl, M. & Schumm, T. Radioluminescence and photoluminescence of Th:CaF₂ crystals. *Sci. Rep.* **5**, 15580 (2015).
- Utter, S. B. et al. Reexamination of the optical gamma ray decay in ^{229}Th . *Phys. Rev. Lett.* **82**, 505–508 (1999).
- Masuda, T. et al. X-ray pumping of the ^{229}Th nuclear clock isomer. *Nature* **573**, 238–242 (2019).
- Verlinde, M. et al. Alternative approach to populate and study the ^{229}Th nuclear clock isomer. *Phys. Rev. C* **100**, 024315 (2019).
- NuDat 3 Database* (National Nuclear Data Center, 2023); <https://www.nndc.bnl.gov/nudat3/>.
- Stellmer, S., Schreitl, M., Kazakov, G. A., Sterba, J. H. & Schumm, T. Feasibility study of measuring the ^{229}Th nuclear isomer transition with ^{233}U -doped crystals. *Phys. Rev. C* **94**, 014302 (2016).
- Hofsäss, H. & Lindner, G. Emission channeling and blocking. *Phys. Rep.* **201**, 121–183 (1991).
- Wahl, U. et al. Position-sensitive si pad detectors for electron emission channeling experiments. *Nucl. Instrum. Meth. Phys. Res. A* **524**, 245–256 (2004).
- Silva, M. R., Wahl, U., Correia, J. G., Amorim, L. M. & Pereira, L. M. C. A versatile apparatus for on-line emission channeling experiments. *Rev. Sci. Instrum.* **84**, 073506 (2013).
- Borge, M. J. G. & Jonson, B. ISOLDE past, present and future. *J. Phys. G: Nucl. Part. Phys.* **44**, 044011 (2017).
- Rubloff, G. W. Far-ultraviolet reflectance spectra and the electronic structure of ionic crystals. *Phys. Rev. B* **5**, 662–684 (1972).
- Thomas, J., Stephan, G., Lemonnier, J. C., Nisar, M. & Robin, S. Optical anisotropy of MgF_2 in its UV absorption region. *Phys. Stat. Sol. (B)* **56**, 163–170 (1973).
- Ziegler, J. F., Ziegler, M. & Biersack, J. Srim - the stopping and range of ions in matter (2010). *Nucl. Instrum. Meth. Phys. Res. B* **268**, 1818–1823 (2010). 19th International Conference on Ion Beam Analysis.
- Beeks, K. *The Nuclear Excitation of Thorium-229 in the CaF₂ Environment*. PhD thesis, TU Wien (2022).
- Evaluated Nuclear Structure Data File* (National Nuclear Data Center, 2023); <https://www.nndc.bnl.gov/ensdf/>.
- David-Bosne, E. et al. A generalized fitting tool for analysis of two-dimensional channeling patterns. *Nucl. Instrum. Meth. Phys. Res. B* **462**, 102–113 (2020).
- Pereira, L., Vantomme, A. & Wahl, U. in *Characterisation and Control of Defects in Semiconductors: Characterizing Defects with Ion Beam Analysis and Channeling Techniques* (ed. Tuomisto, F.) Ch. 11 (The Institution of Engineering and Technology, 2019).
- Kikunaga, H. et al. Half-life estimation of the first excited state of Th-229 by using alpha-particle spectrometry. *Phys. Rev. C* **80**, 034315 (2009).
- Tkalya, E. V., Zherikhin, A. N. & Zhudov, V. I. Decay of the low-energy nuclear isomer $^{229\text{m}}\text{Th}^m(3/2^-, 3.5 \pm 1.0 \text{ eV})$ in solids (dielectrics and metals): a new scheme of experimental research. *Phys. Rev. C* **61**, 064308 (2000).

Publisher's note Springer Nature remains neutral with regard to jurisdictional claims in published maps and institutional affiliations.

Springer Nature or its licensor (e.g. a society or other partner) holds exclusive rights to this article under a publishing agreement with the author(s) or other rightsholder(s); author self-archiving of the accepted manuscript version of this article is solely governed by the terms of such publishing agreement and applicable law.

© The Author(s), under exclusive licence to Springer Nature Limited 2023

Methods

Radioactive ion beam production and implantation

Radioisotopes are produced by a 2 μA proton beam at 1.4 GeV impinging on a uranium carbide target. High temperatures (about 2,000 °C) lead to diffusion of the nuclear-reaction products towards the material boundary and subsequent effusion to the hot cavity ion source region, where surface ionization is used to create singly charged ions. The beam is accelerated to 30 keV and mass separated to obtain constituents of a specific isobar A (ref. 37). The radioactive ion beam is implanted into one of the five crystals mounted on the sample holder wheel. After implantation the wheel is turned by 180° to transfer the sample from its implantation position to the spectroscopy position facing the entrance slit of the VUV spectrometer at a distance of about 3 mm. Typical γ -ray spectra of the $A = 229$ and $A = 230$ decay chains recorded during implantation are shown in Extended Data Fig. 1. From the time evolution during implantation of specific lines of known intensity, the implanted beam composition is deduced. Extended Data Table 1 summarizes the characteristics of the $A = 229$ and $A = 230$ isobaric chain. During data collection with the 50-nm thick CaF_2 crystal, the production rate is a factor of 3 lower compared to the ones reported in the table. From β -decay studies, the total branching ratio feeding the isomer directly and indirectly in the β decay of ^{229}Ac has been determined to be between 14 and 93% (refs. 21,31).

Large-bandgap crystals

Data on the large-bandgap crystals used in this study are summarized in the Extended Data Table 2. The 5 mm MgF_2 and 5, 0.7 and 0.5 mm CaF_2 are commercially available VUV-grade crystals, polished by the manufacturer.

Before the VUV-spectroscopy measurements, the crystal surface was wiped with isopropanol, because our tests revealed that this enhanced their transmission (order of 10% improvement), probably due to removal of surface contaminants introduced during polishing and handling. Before the emission channelling measurements, the crystals were wiped with acetone, as a preemptive measure, to remove debris that could cause electron scattering. The growth of the 50 nm CaF_2 thin film is described in the following paragraph. This thin-film crystal is used as grown, without further surface treatment. Emission of VUV photons from $^{229\text{m}}\text{Th}$ is observed for all crystals.

The CaF_2 thin film is grown using a Riber 49 molecular beam epitaxy reactor on a Si(111) substrate with a thickness of 0.75 mm. The CaF_2 molecular beam is obtained by electron beam evaporation of a CaF_2 target. The flux is calibrated by using a quartz crystal microbalance, and the stability of the CaF_2 beam is ensured by a real time mass spectrometer partial pressure signal with feedback loop. A calibrated optical pyrometer is used to monitor the wafer surface temperature during the growth. Before loading into the molecular beam epitaxy reactor, a 2% NH_4F wet clean of the Si(111) substrates is performed for 60 s to remove part of the native oxide and organic contamination. After introduction into the growth chamber, the deoxidation step is carefully followed by reflection high-energy electron diffraction (RHEED) and the substrate is heated up to 750 °C leading to the appearance of a strong 7×7 surface reconstruction for the Si(111) substrate. In the present study, a CaF_2 thin film with a thickness of 50 nm is epitaxially grown at high temperature (740 °C) with a growth rate of 3.5 nm min⁻¹. RHEED and atomic force microscopy characterization of the CaF_2 thin film is shown in Extended Data Fig. 2. The RHEED pattern along the [11-2] direction shows intense streaks, which confirms the epitaxial property of the CaF_2 layer. The surface morphology of the CaF_2 layer is atomically smooth (r.m.s. roughness of less than 4 Å) with the presence of steps and terraces, originating from the step-flow growth mode induced by the high growth temperature.

Emission channelling

The emission channelling technique is based on the interaction between the electrons emitted on decay of a radioactive isotope and

the periodic Coulomb potential of the host crystal, inducing channelling and blocking effects along the main crystallographic axes and planes. The resulting angle-dependent emission yield is measured using a position-sensitive silicon pad detector^{35,36}, producing two-dimensional electron emission patterns. Because the emission anisotropy is strongly dependent on the position within the crystal lattice from where the electrons are emitted, it allows us to identify which lattice sites are occupied by the implanted radioactive ions and to quantify the respective occupation fractions. The electron emission patterns are measured along various major crystallographic axes, by rotating the sample holder with a three-axis goniometer. At least two axes are required for unambiguous lattice site identification; typically, four axes are measured. Identification and quantification of the occupied lattice sites are obtained by numerically fitting measured and simulated emission patterns. The simulated patterns are calculated for various high-symmetry lattice sites using the Manybeam code³⁴. Each measured pattern is then fitted with a linear combination of simulated sites⁴³ from where the occupation fractions are obtained.

VUV spectroscopy

A Czerny–Turner mount grating monochromator with a 100 × 100 mm plane grating and a sinusoidal ruling of 4,000 lines per mm combined with a F/1.245° off-axis parabolic collimation mirror with a focal length of 119 mm is used (Extended Data Fig. 3). The device has a magnification of $M = 1.5$ and the exit slit close to the detector is set accordingly. A Hamamatsu R8487 solar-blind photomultiplier tube detector with a quantum detection efficiency of 19% at 150 nm is operated in single photon counting mode to detect diffracted photons passing the exit slit. The wavelength is set by rotation of the grating with a linear stepper motor driving a crankshaft and a linear wavelength calibration relation between the motor position and the wavelength holds. The device is scanned from lower to higher wavelengths and the counts observed on the detector are recorded with a CAEN N6730 data acquisition unit. The grating drive offers a reproducibility of the grating position corresponding to a wavelength uncertainty of smaller than 0.18 nm in the first diffraction order when scanned over a large spectral range.

A plasma light source operated with a nitrogen-oxygen gas mixture is mounted behind the crystal in spectroscopy position, emitting a collimated beam of light into the spectrometer with a wavelength spectrum consisting of several non-resolved multiplets of atomic transitions. An oxygen multiplet of transitions at 130.2168, 130.4858 and 130.6029 nm together with a multiplet of nitrogen transitions at 149.2625, 149.2820 and 149.4675 nm and a nitrogen multiplet at 174.2731 and 174.5249 nm are used for calibration. To validate the calibration, the single 146.96 nm line in the spectrum of a cold krypton-xenon plasma light source (Excitech GmbH E-Lux) is used. The wavelength linewidth of the spectrometer is composed of a minimal achievable resolution for a close-to-diffraction-limited entrance slit settings (10 μm), dominated by the optical aberrations of the system, and a roughly linear increase of the linewidth with slit size. Experimentally, full-width at half-maximum linewidths of roughly 2.5 and 5.5 nm are observed for 0.5 and 3 mm entrance slits, respectively.

Next to the contribution from the reproducibility of the grating position mentioned above, two more contributions to the systematic uncertainty of the wavelength calibration have been identified. (1) The calibration light source is positioned between 217 and 350 mm from the entrance slit. The influence of an off-axis mounting of the source with a deviation of up to 1° is calculated and results in a systematic shift of the wavelength calibration of less than 0.15 nm. (2) The implanted radioactive beam profile and therefore the distribution of the light emission in the crystal remains poorly known. Typical radioactive beam spot sizes are of the order of a few mm (full-width at half-maximum) in diameter. The systematic effect of different light source distributions on the observed wavelengths for entrance slit settings of far more than 10 μm has been estimated by simulating the influence of the different

light source distributions on the sample crystal for several entrance slit settings. Using slit settings equal to or less than 0.5 mm, the shift of the observed wavelength is less than 0.33 nm.

The total systematic uncertainty for slit settings equal to or less than 0.5 mm (1 σ confidence level), including the systematic effect of the wavelength calibration light source, the implantation beam profile and the grating drive reproducibility amounts in a conservative estimate to less than 0.41 nm.

The observed wavelength spectra around 148.7 nm consist of three components: (1) the detector dark-count rate is constant over time and less than 1 s^{-1} , (2) the peak of the radiative decay of $^{229\text{m}}\text{Th}$ and (3) the continuous Cherenkov background induced by relativistic electrons from the radioactive decay of ^{229}Ra and ^{229}Ac . A typical spectrum is shown in Fig. 3. The rates from the Cherenkov background need to be scaled with the instantaneous activities of the corresponding fraction and have to be convoluted with the time behaviour of the decay chain elements. The shape of the Cherenkov emission spectrum for the β -decay chains $^{230}\text{Ra} \rightarrow ^{230}\text{Ac} \rightarrow ^{230}\text{Th}$ (I) and $^{229}\text{Ac} \rightarrow ^{229}\text{Th}$ (II) is calculated using the Frank–Tamm formula²⁸. The obtained background spectrum from the $A = 230$ decay chain (I) around 149 nm is due to the Cherenkov spectrum altered by the wavelength-dependent efficiency of the instrument (the wavelength bandpass) and by the time dependence of the instantaneous β activity at $A = 230$. The Cherenkov spectrum altered by the wavelength bandpass can be described by a third-order polynomial. The shape of the ^{229}Ac background spectrum (II) is obtained by scaling the polynomial with the ratio of the calculated pure Cherenkov emission spectra and correcting with the instantaneous activity at $A = 229$.

The $A = 229$ spectra are fitted as a linear combination of the ^{229}Ac Cherenkov background (altered by the wavelength bandpass) scaled with the instantaneous actinium activity, a Gaussian peak scaled with the instantaneous thorium isomer activity and a constant dark-count background. Figure 3 shows the background and the isomeric radiative decay peak fitted to an observed spectrum. Narrow and broad linewidth scans used for the wavelength measurements are recorded sufficiently long after the end of implantation, such that the ^{229}Ra Cherenkov background component vanishes, the $^{229\text{m}}\text{Th}$ activity is saturated and its time dependence follows the simple exponential time behaviour of the ^{229}Ac activity.

Extraction of the half-life

The spectrometer is continuously scanned from 133 to 160 nm with a 2-mm-wide entrance slit setting and spectra are recorded. The amplitude of the observed photon peak and the contribution strengths of the radium and actinium Cherenkov emission are extracted from a fit (see the section VUV spectroscopy and compare the inset of Fig. 2 for a sample fit).

The time dependence of the isomeric decay activity is fitted using a system of Bateman equations of the $A = 229$ decay chain. The relative strength of the implantation beam constituents ^{229}Fr , ^{229}Ra and ^{229}Ac and their half-lives are fixed to the results from γ spectroscopy (Extended Data Fig. 1) and the literature values (Extended Data Table 1), respectively. Next to the half-life of the isomer that is included as a free fitting parameter, a scaling factor is used to adjust the calculated isomer activity to describe the data. The scaling factor results from a product of the fraction of embedded $^{229\text{m}}\text{Th}$ nuclei that decays by means of radiative decay, the total efficiency of the VUV setup and the total feeding probability of the isomer in the β decay of ^{229}Ac . This scaling factor does not change the overall shape of the fit.

On the basis of the simulated relative Cherenkov photon emission strength in the decay of ^{229}Ra and ^{229}Ac , the relative total Cherenkov photon emission rate is obtained from the activities of both decay chain elements after the end of implantation. This rate is scaled with a coefficient, that takes into account the efficiency of the VUV spectrometer for Cherenkov radiation. Figure 2 shows good agreement between the

observed background temporal behaviour and the expected Cherenkov photon emission contributions.

The given uncertainty constitutes a conservative estimate and includes the following contributions: a statistical uncertainty of 79 s is obtained from the Markov chain Monte Carlo optimization. A variation of the ratio of implantation rates of ^{229}Fr to ^{229}Ra by an order of magnitude compared to the experimentally determined value from γ data and a conservative uncertainty of 120 s on the period between the end of implantation and the start of the first measurement result in a 5 and 53 s uncertainty, respectively. Systematic effects resulting from the need to continuously scan the instrument for wavelength spectra recording and the resulting limited amount of data at the isomer's emission wavelength are estimated using a bootstrapping technique removing one data point at the time. The largest half-life deviation from the result with the full dataset, 35 s, has been added to this conservative uncertainty estimate.

Ratio of radiative decaying versus embedded $^{229\text{m}}\text{Th}$ isotopes

To estimate the ratio between the number of $^{229\text{m}}\text{Th}$ decaying by means of radiative decay versus the number of embedded $^{229\text{m}}\text{Th}$ after β decay of ^{229}Ac , several experimental parameters need to be considered of which for some only estimates are available. A conservative lower limit is obtained using data from a 7,080-s long implantation in the CaF_2 5 mm resulting in a VUV count rate of 12 s^{-1} and $1.2 \times 10^6 \text{ Bq}$ ^{229}Ac source strength at 5,400 s after the end of the implantation, combined with the following criteria.

For a crystal implantation surface located at a distance of 3 mm from the slit with a 3 mm opening and a point-like light source at its centre, the solid angle for photon collection is 1.3%. The first-order diffraction efficiency at 150 nm of the grating used in this work is specified by the supplier to be 40% and the quantum detection efficiency of the detector 19%. A total detection efficiency of isotropically emitted photons from a point source at the centre of the crystal implantation surface is roughly equal to 0.1% at 149 nm. Typically the radioactive ion beams from ISOLDE have beam profiles with an approximate full-width half-maximum of the intensity distribution of a few mm, however, these conditions change during radioactive beam tuning and the optimization procedure applied in between the different measuring campaigns. Therefore, the overlap of the implanted beam profile with the region on the crystal implantation surface that is imaged through the $3 \times 10 \text{ mm}$ rectangular entrance slit on the spectrometer, is conservatively estimated to be less than or equal to 100%. The large-bandgap material leads to absorption of photons in the bulk and crossing the surface. Because of the small implantation depth, the VUV photons pass a limited amount of bulk material and the surface facing the entrance slit. The transmissions of the large-bandgap crystals are tested and transmission of VUV photons through the CaF_2 crystals vary between 10 and 80% at 149 nm. For the current estimate, less than 100% is assumed.

This leads to a lower limit of the ratio between the number of $^{229\text{m}}\text{Th}$ decaying by radiative decay versus the number of embedded $^{229\text{m}}\text{Th}$ after β decay of ^{229}Ac of greater than or equal to 1 or 7% using the limits of the ^{229}Ac β branching ratio to $^{229\text{m}}\text{Th}$ values of 93 and 14%, respectively³¹. Other implantation cycles with smaller slit settings or other crystals reveal consistent results.

Data availability

The data that support the findings of this study are available from the corresponding author upon reasonable request. Source data are provided with this paper.

Acknowledgements We thank the ISOLDE collaboration and technical group at CERN for their extensive support and assistance. This work has received funding from Research Foundation Flanders (FWO, Belgium), from grant no. GOA/2015/010 (BOF KU Leuven) and from FWO and

F.R.S.-FNRS under the Excellence of Science (EOS) programme (grant no. 40007501), the Portuguese Foundation for Science and Technology (FCT, project no. CERN/FIS-TEC/0003/2019), the Austrian Science Fund (FWF) project no. I5971 (REThoriC), the European Union's Horizon 2020 research and innovation programme under the ENSAR2 grant agreement no. 654002, under the Marie Skłodowska-Curie grant agreement no. 101026762 and the European Research Council (ERC) under the Thorium Nuclear Clock agreement no. 856415 and under the LRC agreement no. 819957.

Author contributions P.V.D., M.H., L.M.C.P., Y.K., S.R., M.V., S.K., J.M. and A.V. conceived and planned the experiments. S.K. developed the VUV setup with help from H.D.W. and P.V.D.B. S.K. and P.C. prepared the VUV-spectroscopy experiments. J.M., U.W. and L.M.C.P. prepared the emission channelling experiments. C.M. grew the CaF₂ thin films. S.K., J.M., M.A.-K., S.B., K.B., P.C., K.C., A.C., T.E.C., J.M.C., R.F., S.G., R.H., N.H., M.L., R.L., G.M., S.R., S.S., P.G.T., P.V.D., S.M.T., U.K., R.V. and U.W. performed the measurements. S.K., S.B., P.C. and S.S. analysed the

VUV-spectroscopy data. J.M. analysed the emission channelling data. S.K., J.M., L.M.C.P., S.S. and P.V.D. prepared the manuscript. All authors provided critical feedback and helped shape the research, analysis and manuscript. This article results from the PhD thesis work of S.K. and J.M.

Competing interests The authors declare no competing interests.

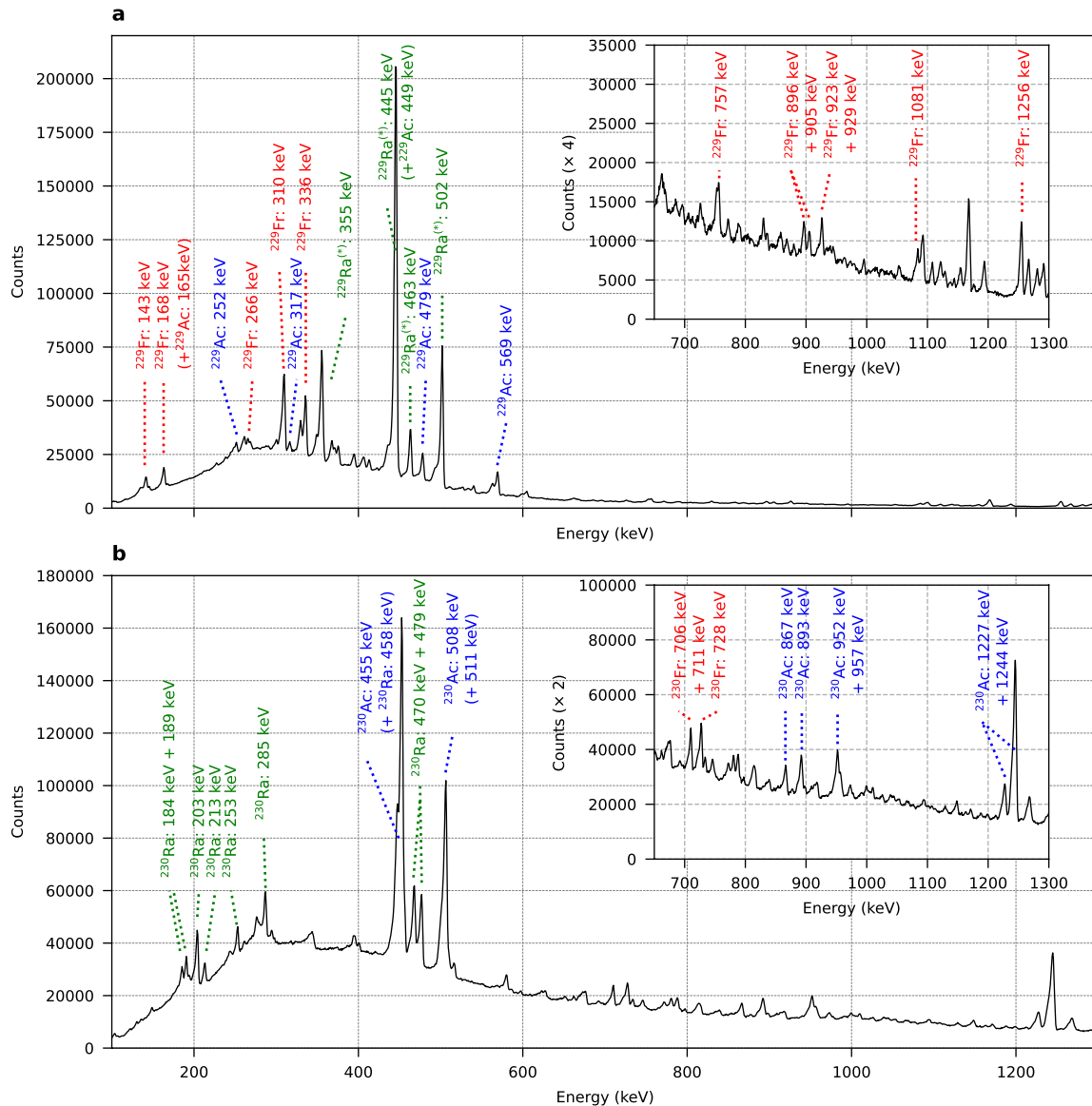
Additional information

Supplementary information The online version contains supplementary material available at <https://doi.org/10.1038/s41586-023-05894-z>.

Correspondence and requests for materials should be addressed to Sandro Kraemer.

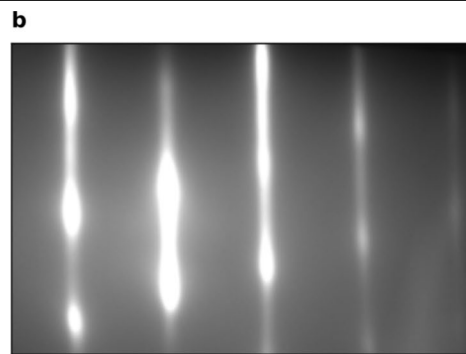
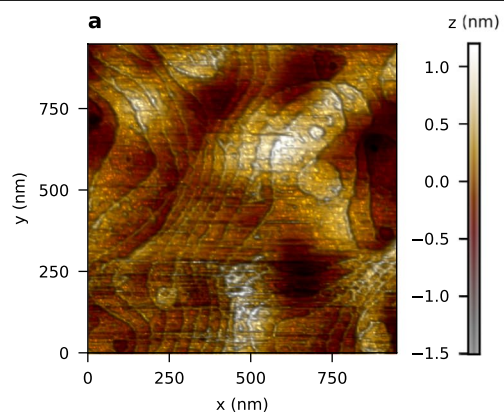
Peer review information *Nature* thanks Iain Moore and the other, anonymous, reviewer(s) for their contribution to the peer review of this work. Peer reviewer reports are available.

Reprints and permissions information is available at <http://www.nature.com/reprints>.

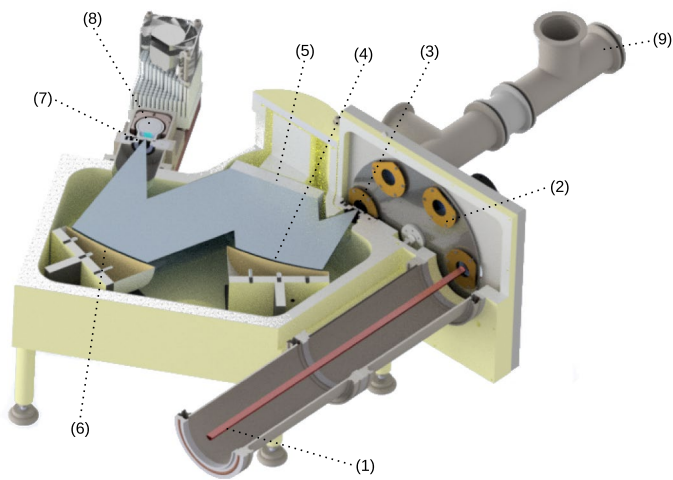


Extended Data Fig. 1 | High-purity germanium detector spectra. Single γ spectra recorded with the HPGe detector for a typical implantation at $A = 229$ (a) and $A = 230$ (b). The main peaks in the spectrum are marked with the

β -decaying isotope and the energy. In this study, new γ lines in the decay of ^{229}Ra were identified, these tentative assignments are indicated with an asterisk. The inset shows the high-energy part of the spectrum with smaller peaks.



Extended Data Fig. 2 | Characteristics of the CaF₂ thin-film crystal surface. An atomic force microscopy (AFM) image of the surface of the CaF₂ thin film (**a**) and a reflection high-energy electron diffraction (RHEED) pattern along [11-2] azimuthal direction (**b**) are shown.



Extended Data Fig. 3 | Vacuum-ultraviolet spectroscopy setup. The implantation beam (1), target wheel with large-bandgap crystals (2), entrance slit (3), parabolic collimation mirror (4), diffraction grating (5), parabolic camera mirror (6), detector slit (7) photomultiplier detector (8) and plasma

VUV-photon source used for calibration (9) are shown. The setup includes additionally γ -radiation detectors placed close to the implantation position of the crystal.

Extended Data Table 1 | Characteristics of the isobaric β -decay chains

Isotope	Half-life*	γ energy (intensity ^{†,‡}) keV	Q_{β} value [†] keV	Production rate pps [§]
²²⁹ Fr	50.2(20) s	336 (21.5%) 1256 (3.7%)	3250(40)	$1.6 \cdot 10^5$
²²⁹ Ra	4.0(2) min		1810(30)	$1.8 \cdot 10^{6 }$
²²⁹ Ac	62.7(5) min	569 (2.3%)	1170(30)	$\leq 1 \cdot 10^5\#$
²²⁹ Th	7932(28) y			
²³⁰ Fr	19.1(5) s	707 (1.86%) 711 (16.9%)	4983(32)	$2.5 \cdot 10^4$
²³⁰ Ra	93(2) min	252 (0.85%) 285 (1.6%)	710(300)	$3.0 \cdot 10^6$
²³⁰ Ac	122(3) s	1227 (1.0%) 1244 (3.6%)	2943 [☆]	$\leq 1 \cdot 10^5$
²³⁰ Th	75400(300) y		4770.0 (15)	
²³¹ Fr	17.6(6) s		3864(14)	
²³¹ Ra	104(1) s		2454(17)	
²³¹ Ac	7.5(1) min		1947(13)	
²³¹ Th	25.52(1) h		391.5(15)	

The A=229, A=230 and A=231 β -decay chains used in this study are listed. *Value is taken from³². †Value(s) are taken from⁴². ‡Absolute γ -ray intensity per β decay is given. §The uncertainty on the production rate is estimated at 20%, the implantation-to-implantation variation of the beam intensity rises up to a factor of 3. || γ -ray intensities from ²²⁹Ra are not known from literature, the production rate therefore is determined using ²²⁹Ac γ rays observed after the decay of ²²⁹Ra. #The lower limit is deduced from the time evolution of the 569 keV γ ray in the decay of ²²⁹Ac.

*No uncertainties are given in the database.

Article

Extended Data Table 2 | List of large-bandgap crystals

Material	Manufacturer	Thickness	Surface
MgF ₂	Thorlabs Inc.	5 mm	Polished up to 20-10 Scratch-Dig
CaF ₂	Thorlabs Inc.	5 mm	Polished up to 40-20 Scratch-Dig
CaF ₂	MaTeck GmbH	0.7 mm	Chem.-mechan. polished with R _t < 10 nm.
CaF ₂	CRYSTAL GmbH	0.5 mm	Chem.-mechan. polished with R _t < 2 nm.
CaF ₂	(grown by the authors)	50 nm	No treatment.

The manufacturer, thickness and surface treatment of the different crystals used in this study are listed.